

Accepted Manuscript

A finite element model for fluid–structure interaction problems involving closed membranes, internal and external fluids

Pavel B. Ryzhakov, Eugenio Oñate

PII: S0045-7825(17)30594-7
DOI: <http://dx.doi.org/10.1016/j.cma.2017.08.014>
Reference: CMA 11553

To appear in: *Comput. Methods Appl. Mech. Engrg.*

Received date: 19 May 2017
Revised date: 18 July 2017
Accepted date: 10 August 2017

Please cite this article as: P.B. Ryzhakov, E. Oñate, A finite element model for fluid–structure interaction problems involving closed membranes, internal and external fluids, *Comput. Methods Appl. Mech. Engrg.* (2017), <http://dx.doi.org/10.1016/j.cma.2017.08.014>

This is a PDF file of an unedited manuscript that has been accepted for publication. As a service to our customers we are providing this early version of the manuscript. The manuscript will undergo copyediting, typesetting, and review of the resulting proof before it is published in its final form. Please note that during the production process errors may be discovered which could affect the content, and all legal disclaimers that apply to the journal pertain.



A finite element model for fluid-structure interaction problems involving closed membranes, internal and external fluids

Pavel B. Ryzhakov¹ and Eugenio Oñate^{1,2}

¹Centre Internacional de Mètodes Numèrics en Enginyeria (CIMNE)

Edifici C1 Campus Nord UPC C/ Gran Capità, S/N 08034 Barcelona, Spain

²Universitat Politècnica de Catalunya - BarcelonaTech, 08034 Barcelona, Spain

Corresponding author email: pryzhakov@cimne.upc.edu

Abstract

In this paper we propose a Finite Element model for analyzing closed membranes ("bags") interacting with internal and external (surrounding) fluids. The approach is based on embedding a Lagrangian monolithic model describing the membrane containing an internal fluid into an Eulerian external fluid model. The combination of kinematic frameworks allows us to accurately track the location of the membrane and naturally represent flow variables discontinuities across it. In order to obtain stable coupling for membrane materials with low density, a slight fluid compressibility is assumed. The coupling between the membrane and the internal fluid is automatically accounted for by a monolithic set-up. The filled membrane and the external fluid are coupled in a Dirichlet-Neumann fashion. The model is validated in several numerical examples and its potential application to a civil engineering problem of coast protection via water-filled bag reefs is shown.

1. Introduction

Fluid-membrane interaction is found many engineering problems and bio-systems. Examples of the latter include lungs, blood vessels and urinary bladder. Among engineering systems one can mention vehicle airbags, water-filled bags, parachutes, sails, tents, inflatable civil engineering structures and many others. One can distinguish between problems involving "open membranes" (such as sails) and those dealing with "closed membranes" (such as bags or balloons), where no direct interaction between the fluid filling the membrane and the surrounding fluid takes place and the two fluids may be different. The objective of the present paper is to develop an ad-hoc model particularly suitable for analysis of "closed membranes" interacting with both the surrounding and the internal fluids.

While being a particular case of fluid-structure interaction, fluid-membrane interaction problems are characterized by the specific nature of the solid. A membrane is a spatial structure that is intrinsically two-dimensional (2D). It resists tensile stresses only and lacks (or has very little) flexural stiffness. A membrane reacts to applied loads by adjusting its spatial configuration finding the best-possible shape for resisting the external loading. Fundamentals of finite element formulations for membrane structures can be consulted in e.g. [1],[2],[3],[4],[5].

Numerical modeling of fluid-membrane interaction is a challenging task due to several reasons. High flexibility of membranes results in large domain distortions and geometric non-linearity of the coupled problem. Typically low density of membrane materials leads to the spurious "added-mass-effect", encountered in incompressible fluid-structure interaction problems where the density ratio of the fluids and the solid is close to one [6], [7], [8]. Very small thickness of membranes introduces an additional challenge: considering a membrane interacting with fluids at both its faces, flow variables discontinuity across the fluid-membrane interface must be represented over a region with a nearly zero thickness.

A common technique for solving fluid-membrane interaction problems consists in embedding a Lagrangian structural model into an Eulerian mesh, the latter being used to calculate the dynamics of the fluid (Fig. 1(a)). One solves the flow equations on a fixed mesh and projects the stresses onto the structure, which is solved by a separate structural solver. The deformation of the structure, in turn, provides the location of the discontinuity and the velocity boundary conditions for the fluid problem. Examples of this overall setting can be found in [9], [10], [11].

Discontinuity of the flow variables across the fluid-membrane interface is usually modeled on fixed grids by enriching the fluid elements intersected by the membrane with discontinuous shape functions, or by introducing element splitting. For alleviating the added mass effect multiple remedies have been proposed (see e.g. [8]), the most common one being the dynamic under-relaxation procedure [12], where an additional equation for improved prediction of the fluid-structure interface location is solved, prior to starting the conventional nested fluid-structure iteration loop.

Alternatively, moving grid methods can be applied to solving the entire fluid-membrane problem. In [13] a Lagrangian model for closed membranes containing an internal fluid was presented. The fluid volume was obtained by integrating over the membrane surface and Boyle's law was used to compute air pressure changes due to volume variation. Internal pressure forces were represented by an additional term in the tangent operator.

In [14], [15] the entire computational domain (the solid and the fluid) was discretized using a single matching Lagrangian mesh. The formulation was proposed for a general fluid-structure system using displacements as the primary kinematic variables. A single monolithic discrete system of equations described the coupled system making the interaction an intrinsic feature of the method. In order to avoid mesh distortion, re-meshing was applied to the fluid part of the

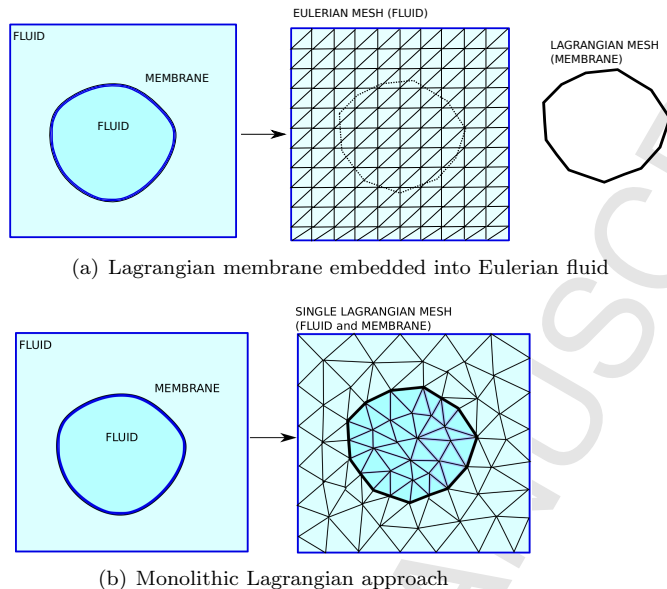


Figure 1: Schematic representation of different kinematic frameworks for the solution of a fluid-structure interaction problem involving closed membranes.

domain, while maintaining the mesh of the structure intact. The uniqueness of degrees of freedom at the interface nodes precluded the possibility of modeling the flow variable discontinuities across the fluid-membrane interface. Thus, the mentioned method cannot be applied to the analysis of membranes interacting with both internal and external fluids.

An extension of the monolithic Lagrangian method to the case of a thin structure interacting with both external and internal fluids was proposed in [16]. In order to represent the discontinuity at the fluid-membrane interface on a single matching grid, the degrees of freedom were duplicated at the interface nodes. Thus, the discontinuity of flow variables (particularly, the pressure) across the structure could be represented. A monolithic Lagrangian setting for fluid-membrane interaction problems is shown in Fig. 1(b).

In the present work we propose a different kinematic setting in order to account for the presence of both external and internal fluids to the closed membrane and to represent the discontinuity across the membrane skin. Our goal is to develop a formulation specifically designed for modeling the interaction of closed membranes filled with water (hereafter called "water bags") or air (airbags) with external fluids. A monolithic Lagrangian fluid-structure formulation is used for modeling the membrane together with the internal fluid adopting the ideas of [14]. However, the external fluid is modeled using a fixed (Eulerian) mesh. The coupling of the Eulerian domain (external fluid) and the Lagrangian domain (internal fluid+membrane) is implemented following the philosophy of

embedded methods. The Lagrangian sub-domain (internal fluid+membrane) moves on top of the fixed Eulerian mesh forcing the external fluid to deform accordingly and receiving the feedback in terms of stresses at the interface boundary. Similarly to the standard embedded approaches, the interface between the external fluid and the membrane is defined by the intersection of the membrane mesh and the Eulerian mesh. The interface between the internal fluid and the membrane is intrinsically tracked by the monolithic Lagrangian model. The difference with conventional Eulerian-Lagrangian embedded models for fluid-membrane interaction is that in our approach membrane and the internal fluid are solved together.

The benefit of the kinematic setting here proposed is the simplicity for representing the discontinuity across the membrane and that re-meshing is restricted to the internal fluid domain only, which reduces the computational cost. This approach can be considered a natural extension of the authors' previous work in the field of fluid-structure interaction [14], [17], [18], [19].

The paper is organized as follows. First, the governing equations for the problem are specified at the continuous level. Then the discrete version of the governing equations for the external fluid in the Eulerian framework is defined. Afterwards, the discrete governing equations for the membrane and the internal fluid in the Lagrangian framework are derived. Coupling of the Eulerian and Lagrangian models is specified and the overall coupled solution algorithm is presented. The paper concludes with several numerical examples for validating the model and highlighting its benefits for solving a practical problem in coastal engineering.

2. Equations of motion at continuum level

A fluid-solid interaction model requires defining the governing equations for the fluid and for the solid as well as the boundary conditions at the common interface and the outer boundaries. Fig. 2 shows the nomenclature and notation used here for the domains and corresponding boundaries. The fluid domain Ω^f is split by the solid (membrane) domain Ω^s into an internal fluid domain Ω^{fi} and an external fluid domain Ω^{fe} . The interface boundary Γ^I coincides with the membrane domain Ω^s .

Fluid. Considering Newtonian nearly incompressible behavior, the governing equations for the fluid domain Ω^f can be written as:

$$\rho \frac{D\mathbf{v}}{Dt} - \mu \nabla \cdot (\nabla \mathbf{v} + \nabla^T(\mathbf{v})) + \nabla p = \rho \mathbf{g} \quad \text{in } \Omega^f \quad (1)$$

$$\frac{Dp}{Dt} = -\kappa \nabla \cdot \mathbf{v} \quad \text{in } \Omega^f \quad (2)$$

where $\frac{D}{Dt}$ is the material time derivative of the velocity vector, p is the pressure, t is time, \mathbf{g} is the body force, ρ is the fluid density and μ is the dynamic viscosity of the fluid.

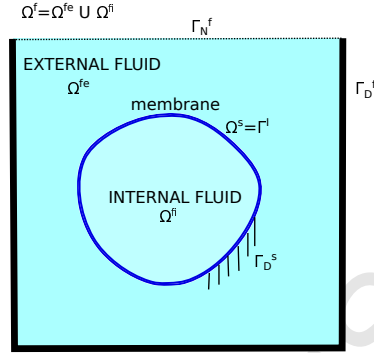


Figure 2: Schematic representation of a fluid-membrane interaction problem. Domains and boundaries

Note that the mass conservation equation is relaxed here as this is known to alleviate the added-mass effect present in FSI simulations in case of applying a strictly divergence-free condition in the fluid domain ([20], [21], [22], [14], [23], [17]).

Membrane. The conservation of linear momentum for the membrane is written in the total Lagrangian form, considering the undeformed configuration \mathbf{X} as a reference:

$$\rho \mathbf{a} = \nabla_{\mathbf{X}} \cdot \mathbf{P} + \mathbf{f}_{ext} \quad \text{in } \Omega^s \quad (3)$$

where \mathbf{a} is the acceleration, \mathbf{P} is the nominal stress tensor, $\nabla_{\mathbf{X}} \cdot \mathbf{P} = \frac{\partial P_{ij}}{\partial X_j}$ is the Lagrangian divergence operator, \mathbf{f}_{ext} is the external force and ρ is the density of the continuum. It can be rewritten in terms of displacements as

$$\rho \frac{\partial^2 \mathbf{d}}{\partial t^2} - \nabla_{\mathbf{X}} \cdot \mathbf{P} = \mathbf{f}_{ext} \quad \text{in } \Omega^s \quad (4)$$

where $\mathbf{d} = \mathbf{x} - \mathbf{X}$, and \mathbf{X} and \mathbf{x} are the current and initial (undeformed) positions of a given point, respectively.

The constitutive equation in the total Lagrangian reference frame is commonly defined as a relation between the 2nd Piola-Kirchhoff stress tensor \mathbf{S} and the Green-Lagrange strain tensor \mathbf{E} defined as

$$\mathbf{E} = \frac{1}{2} (\mathbf{F}^T \cdot \mathbf{F} - \mathbf{I}) \quad (5)$$

where $\mathbf{F} = \frac{\partial \mathbf{x}}{\partial \mathbf{X}}$ is the deformation gradient. Using the nominal stress for the constitutive equations is inconvenient due to its lack of symmetry. However, once the 2nd Piola-Kirchhoff stress has been evaluated (using the constitutive equation $\mathbf{S} = \mathbf{S}(\mathbf{E})$), the nominal stress is obtained as

$$\mathbf{P} = \mathbf{S} \cdot \mathbf{F}^T \quad (6)$$

Note that by now the equations are written for a general 3D continuum solid and no assumptions corresponding to specific features of membranes have been made. Also the stress-strain relationship has not been specified yet.

Boundary conditions. Homogeneous Dirichlet boundary conditions are prescribed at the outer boundary of the fluid. If free fluid surface is present, the homogeneous Neumann ("free-surface") condition is prescribed there. The corresponding boundary conditions can be written as:

$$\mathbf{v} = 0 \quad \text{at } \Gamma_D^f \quad (7)$$

$$\boldsymbol{\sigma} \cdot \mathbf{n} = 0 \quad \text{at } \Gamma_N^f \quad (8)$$

where \mathbf{n} is the outer unit normal vector to Γ_N .

For the fixed boundaries of the solid, a homogeneous Dirichlet condition is prescribed as:

$$\mathbf{d} = 0 \quad \text{at } \Gamma_D^s \quad (9)$$

$$(10)$$

At the interface between the fluid and the solid the no-slip condition (continuity of velocity) and continuity of stresses are prescribed as:

$$\mathbf{v} = \dot{\mathbf{d}} \quad \text{at } \Gamma^I \quad (11)$$

$$\boldsymbol{\sigma}_f \cdot \mathbf{n} = \boldsymbol{\sigma}_s \cdot \mathbf{n} \quad \text{at } \Gamma^I \quad (12)$$

Noting that for a membrane the solid/internal fluid and the solid/external fluid interfaces coincide, one can re-write the above interface conditions as (index fi and fe stand for external and internal fluid domains Ω^{fi} and Ω^{fe} , respectively):

$$\mathbf{v}_{fe} = \dot{\mathbf{d}} = \mathbf{v}_{fi} \quad \text{at } \Gamma^I \quad (13)$$

$$\boldsymbol{\sigma}_{fe} \cdot \mathbf{n} = \boldsymbol{\sigma}_s \cdot \mathbf{n} + \boldsymbol{\sigma}_{fi} \cdot \mathbf{n} \quad \text{at } \Gamma^I \quad (14)$$

3. Finite Element model

Partitioning. Let us consider that the external fluid is discretized with a fixed (Eulerian) mesh, while the internal fluid and the membrane are discretized together by a moving (Lagrangian) grid. This setting defines the particular type

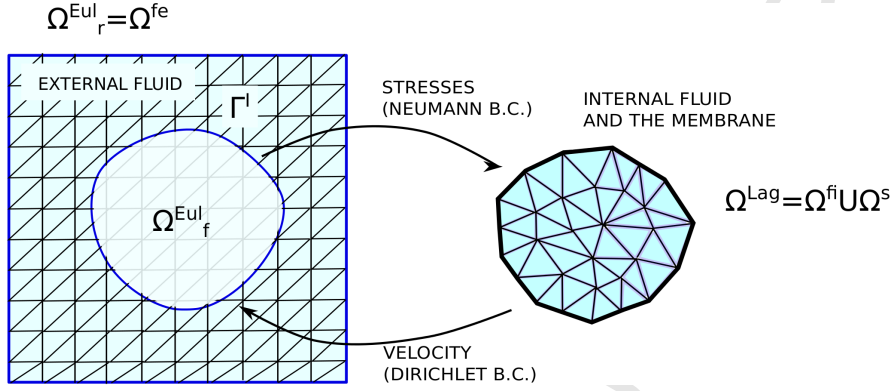


Figure 3: Proposed embedded partitioning: Eulerian domain (external fluid) and Lagrangian domain (membrane+internal fluid).

of the embedded coupling proposed here ¹. This partitioning is indicated in Fig. 3.

As shown in Fig. 3 the Eulerian mesh is split into two parts by the membrane.

The first one (in shade) corresponds to the external fluid to be solved in the Eulerian mesh. It will be called the "real Eulerian fluid" and denoted as Ω_r^{Eul} . The second one Ω_f^{Eul} (white) is considered fictitious for the Eulerian mesh and the fluid occupying this sub-domain is modeled on the Lagrangian mesh. Therefore, the elements belonging to the fictitious part of the Eulerian mesh are "switched off". The interface elements, i.e. the ones that are intersected by the membrane are used for imposing the interface Dirichlet boundary condition representing the effect of the moving membrane onto the surrounding (external) fluid. **In order to find the partitioning of the Eulerian domain, the intersections of the Lagrangian surface mesh (Γ_L) with the Eulerian elements is identified. The polygon defined by these intersections provides Γ_I , i.e. the representation of the Lagrangian surface within the Eulerian mesh.**

3.1. Eulerian model (external fluid)

For discretizing the Navier-Stokes equations (Eqs. (1) and (2)) on the Eulerian mesh we shall consider a space discretization using linear velocity-pressure tetrahedra. The finite element approximations of the velocities and the pressure

¹A typical embedded membrane-fluid coupling implies modeling the entire fluid (internal and external) on a single Eulerian mesh, while modeling the membrane on a moving grid.

are:

$$\mathbf{v}(\mathbf{x}, t) = \sum_{I=1}^4 \bar{\mathbf{v}}_I(t) \mathbf{N}_I(\mathbf{x}) = \mathbf{N}^T \begin{pmatrix} \mathbf{v}_{1x} \\ \mathbf{v}_{1y} \\ \mathbf{v}_{1z} \\ \dots \\ \mathbf{v}_{4x} \\ \mathbf{v}_{4y} \\ \mathbf{v}_{4z} \end{pmatrix} \quad (15)$$

$$p(\mathbf{x}, t) = \sum_{I=1}^4 \bar{p}_I(t) N_I(\mathbf{x}) = \mathbf{N}_p^T \begin{pmatrix} p_1 \\ p_2 \\ p_3 \\ p_4 \end{pmatrix} \quad (16)$$

with

$$\mathbf{N} = \begin{pmatrix} N_1 & 0 & 0 & \dots & N_4 & 0 & 0 \\ 0 & N_1 & 0 & \dots & 0 & N_4 & 0 \\ 0 & 0 & N_1 & \dots & 0 & 0 & N_4 \end{pmatrix}^T \quad (17)$$

$$\mathbf{N}_p = (N_1 \quad N_2 \quad N_3 \quad N_4)^T \quad (18)$$

where N_I are the standard linear finite element shape functions, the over-bar in Eqs. (15) and (16) distinguishes the vectors of nodal quantities and I stands for the nodal index.

For the sake of simplicity in this work we will use a Backward Euler time discretization scheme. However, all the arguments presented in the paper hold for any implicit time integration scheme.

The discretized problem in the residual form can be stated as follows. Given $\bar{\mathbf{v}}_n$ and $\bar{\mathbf{p}}_n$ at t_n , find $\bar{\mathbf{v}}_{n+1}$ and $\bar{\mathbf{p}}_{n+1}$ at t_{n+1} as the solution of

$$\bar{\mathbf{r}}_m^{fe} = 0 \quad (19)$$

$$\bar{\mathbf{r}}_c^{fe} = 0 \quad (20)$$

where $\bar{\mathbf{r}}_m$ and $\bar{\mathbf{r}}_c$ are the residua of the momentum and continuity equations, respectively. These are defined as:

$$\bar{\mathbf{r}}_m^{fe} = \mathbf{f}_{ext} - \rho \mathbf{M} \frac{\bar{\mathbf{v}}_{n+1} - \bar{\mathbf{v}}_n}{\Delta t} - \mathbf{K}(\bar{\mathbf{v}}_{n+1}) \bar{\mathbf{v}}_{n+1} + \mu \mathbf{L} \bar{\mathbf{v}}_{n+1} - \mathbf{G} \bar{\mathbf{p}}_{n+1} \quad (21)$$

$$\bar{\mathbf{r}}_c^{fe} = \kappa \Delta t \mathbf{D} \bar{\mathbf{v}}_{n+1} - \mathbf{M}_p (\bar{\mathbf{p}}_{n+1} - \bar{\mathbf{p}}_n) \quad (22)$$

where \mathbf{M} , \mathbf{L} , \mathbf{G} and \mathbf{D} are mass, Laplacian, gradient and divergence matrices, respectively. The pressure mass matrix is distinguished by the "p" subscript. $\bar{\mathbf{v}}$ and $\bar{\mathbf{p}}$ are the nodal velocity and the nodal pressure vectors, respectively and \mathbf{f}_{ext} is the body force vector.

The matrices and vectors are assembled from the element contributions as:

$$\mathbf{M} = \sum_{elem} \int_{\Omega_e} \mathbf{N}\mathbf{N}^T d\Omega \quad (23) \quad \mathbf{L} = \sum_{elem} \int_{\Omega_e} \nabla\mathbf{N}\nabla\mathbf{N}^T d\Omega \quad (24)$$

$$\mathbf{G} = - \sum_{elem} \int_{\Omega_e} \nabla\mathbf{N}\mathbf{N}_p d\Omega \quad (25) \quad \mathbf{f}_{ext} = \sum_{elem} \rho \int_{\Omega_e} \mathbf{N}\mathbf{g} d\Omega \quad (26)$$

$$\mathbf{M}_p = \sum_{elem} \int_{\Omega_e} \mathbf{N}_p\mathbf{N}_p^T d\Omega \quad (27) \quad \mathbf{D} = -\mathbf{G}^T \quad (28)$$

$$\mathbf{K} = \sum_{elem} \left(\rho \int_{\Omega_e} \mathbf{N} (\bar{\mathbf{v}} \cdot \nabla\mathbf{N}) d\Omega + \int_{\Omega_e} (\bar{\mathbf{v}} \cdot \nabla\mathbf{N}) \tau \left(\frac{\rho}{\Delta t} \mathbf{N} + \rho \bar{\mathbf{v}} \cdot \nabla\mathbf{N} \right) d\Omega \right) \quad (29)$$

Note that the second term in the definition of \mathbf{K} corresponds to the convection stabilization according to the SUPG (streamline upwind Petrov-Galerkin) method [24]. The algorithmic stabilization parameter is computed as $\tau = \frac{1}{\frac{h}{2\|\bar{\mathbf{v}}\|} + \frac{h^2}{4\nu}}$, where h is the element size and ν is the kinematic viscosity of the fluid.

For large values of bulk modulus, the numerical solution can have spurious instabilities in the pressure field. A stabilized solution for the pressure can be obtained by modifying Eq. (22) as:

$$\bar{\mathbf{r}}_c = \kappa\Delta t\mathbf{D}\bar{\mathbf{v}}_{n+1} - \left(\mathbf{M}_p^l \bar{\mathbf{p}}_{n+1} - \mathbf{M}_p^c \bar{\mathbf{p}}_n \right) \quad (30)$$

According to this modification, the historical and the present values for the pressure are multiplied by consistent and lumped mass matrices, respectively. The difference between the consistent and the lumped mass matrices is often used as an approximation of the Laplacian operator (typically arising in the continuity equation when applying conventional pressure stabilization schemes). The technique based on difference between the consistent and the lumped mass matrices is similar to the pressure stabilization method proposed in [25]. The details of this technique in the context of quasi-incompressible finite element formulations can be consulted in [14], [26].

The discretized governing system defined by Eqs. (19) and (20) is non-linear due to the dependence of the convection operator on the unknown velocity. It can be solved by any standard iterative procedure. The linearized system solved at every iteration step can be written as:

$$\mathbf{H}^{fe} \begin{pmatrix} \delta\bar{\mathbf{v}} \\ \delta\bar{\mathbf{p}} \end{pmatrix} = \begin{pmatrix} \bar{\mathbf{r}}_m^{fe} \\ \bar{\mathbf{r}}_c^{fe} \end{pmatrix} \quad (31)$$

where the tangent matrix \mathbf{H} is defined as:

$$\mathbf{H}^{fe} = \begin{pmatrix} \frac{\mathbf{M}}{\Delta t} + \rho\mathbf{K} + \mathbf{S}_K + \mu\mathbf{L} & \mathbf{G} \\ \kappa\Delta t\mathbf{D} & \mathbf{M}_p \end{pmatrix} \quad (32)$$

The above equations must be equipped with a boundary condition representing the velocity of the Lagrangian domain boundary in the Eulerian mesh, i.e. $\mathbf{v}_{n+1} - \dot{\mathbf{d}}_{n+1} = 0$ at Γ_I . In [27] it has been shown that minimizing this difference in an integral sense along Γ_I leads to:

$$\int_{\Gamma_I} \mathbf{M} \mathbf{v}_{n+1} d\Gamma = \int_{\Gamma_I} \mathbf{N}^T \dot{\mathbf{d}}_{n+1} d\Gamma \quad (33)$$

This equation is assembled from the elemental contributions of the interface elements, i.e. the elements intersected by Γ_I (see Fig. 4). We propose to treat this constraint explicitly. This can be done assuming that the velocity at the “real” nodes of the interface elements is known and equal to the velocity obtained at the previous time step. Solving Eq. (33) the velocity at the fictitious nodes is obtained (see black dots in Fig. 4), that is consequently applied as the interface Dirichlet boundary condition at the next time step, representing the action of the Lagrangian fluid onto the Eulerian one. For further details regarding the solution of the interface equation the reader is referred to [27].

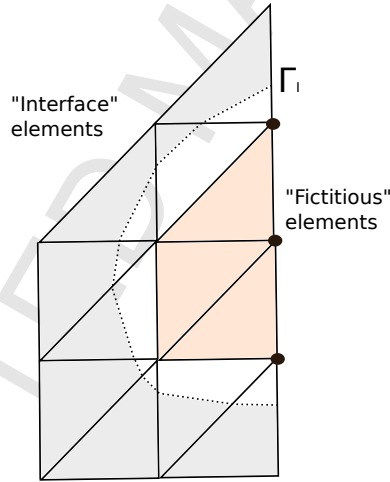


Figure 4: Interface Dirichlet boundary condition.

Once $\delta \bar{\mathbf{v}}$ and $\delta \bar{\mathbf{p}}$ are found, the primary variables are updated as $\bar{\mathbf{v}}_{n+1}^{i+1} = \bar{\mathbf{v}}_{n+1}^i + d\bar{\mathbf{v}}$ and $\bar{\mathbf{p}}_{n+1}^{i+1} = \bar{\mathbf{p}}_{n+1}^i + d\bar{\mathbf{p}}$ (where i is the non-linear iteration index) until convergence is achieved.

3.2. Lagrangian model (membrane and internal fluid)

Membrane. We will derive the finite element model for the membrane starting with the standard assumptions for membrane theory:

- no bending resistance
- plane stress conditions
- normals remain orthogonal to the mid-surface of the membrane

Below a three-dimensional (3D) approach is presented. It facilitates implementing the membrane as a classical total Lagrangian 3D element. The derivation follows the methodology described in [28].

Considering iso-parametric finite elements, the position of a point lying in the mid-surface of a membrane can be written as

$$\mathbf{x}_{mid}(\xi, \eta) = N_I(\xi, \eta)\mathbf{x}_I \quad (34)$$

where $\mathbf{x}_I = (x_I, y_I, z_I)^T$ is the position of the node I , N is the standard linear shape function and ξ and η are the local coordinates in the tangent plane to the mid-surface.

An arbitrary point in a membrane can be expressed as

$$\mathbf{x}(\xi, \eta, \zeta) = N_I(\xi, \eta)\mathbf{x}_I + \frac{t}{2}\zeta\mathbf{n} \quad (35)$$

where ζ is the off-plane direction, \mathbf{n} is the normal to the mid-surface and t is the thickness of the element.

Assuming that the normal is constant in the thickness direction (i.e. $\mathbf{n}(\xi, \eta, \zeta) = \mathbf{n}(\xi, \eta)$) one can obtain the coordinate Jacobian \mathbf{J} using Eq. (35):

$$\mathbf{J} = \begin{pmatrix} \frac{\partial N_I}{\partial \xi} x_I + \left(\frac{t}{2}\zeta \frac{\partial \mathbf{n}}{\partial \xi}\right)_x & \frac{\partial N_I}{\partial \eta} x_I + \left(\frac{t}{2}\zeta \frac{\partial \mathbf{n}}{\partial \eta}\right)_x & \left(\frac{t}{2}\mathbf{n}\right)_x \\ \frac{\partial N_I}{\partial \xi} y_I + \left(\frac{t}{2}\zeta \frac{\partial \mathbf{n}}{\partial \xi}\right)_y & \frac{\partial N_I}{\partial \eta} y_I + \left(\frac{t}{2}\zeta \frac{\partial \mathbf{n}}{\partial \eta}\right)_y & \left(\frac{t}{2}\mathbf{n}\right)_y \\ \frac{\partial N_I}{\partial \xi} z_I + \left(\frac{t}{2}\zeta \frac{\partial \mathbf{n}}{\partial \xi}\right)_z & \frac{\partial N_I}{\partial \eta} z_I + \left(\frac{t}{2}\zeta \frac{\partial \mathbf{n}}{\partial \eta}\right)_z & \left(\frac{t}{2}\mathbf{n}\right)_z \end{pmatrix} \quad (36)$$

Since the membrane deformation is assumed constant over the thickness, one can evaluate the coordinate Jacobians on the mid-surface ($\zeta = 0$). This simplifies the expression, removing the dependence of the solution on the local derivatives of the normal with respect to ξ and η , leading to

$$\mathbf{J} = \begin{pmatrix} \frac{\partial N_I}{\partial \xi} x_I & \frac{\partial N_I}{\partial \eta} x_I & \left(\frac{t}{2}\mathbf{n}\right)_x \\ \frac{\partial N_I}{\partial \xi} y_I & \frac{\partial N_I}{\partial \eta} y_I & \left(\frac{t}{2}\mathbf{n}\right)_y \\ \frac{\partial N_I}{\partial \xi} z_I & \frac{\partial N_I}{\partial \eta} z_I & \left(\frac{t}{2}\mathbf{n}\right)_z \end{pmatrix} \quad (37)$$

Similarly, the reference configuration Jacobian \mathbf{J}_0 can be written as

$$\mathbf{J}_0 = \begin{pmatrix} \frac{\partial N_I}{\partial \xi} X_I & \frac{\partial N_I}{\partial \eta} X_I & \left(\frac{t_0}{2}\mathbf{n}_0\right)_x \\ \frac{\partial N_I}{\partial \xi} Y_I & \frac{\partial N_I}{\partial \eta} Y_I & \left(\frac{t_0}{2}\mathbf{n}_0\right)_y \\ \frac{\partial N_I}{\partial \xi} Z_I & \frac{\partial N_I}{\partial \eta} Z_I & \left(\frac{t_0}{2}\mathbf{n}_0\right)_z \end{pmatrix} \quad (38)$$

Note that \mathbf{n}_0 stands for the normal vector to the mid-surface in the initial configuration.

Introducing two vectors tangent to the mid-surface,

$$\mathbf{g}_\xi = \left(\frac{\partial N_I(\xi, \eta)}{\partial \xi} x_I \quad \frac{\partial N_I(\xi, \eta)}{\partial \xi} y_I \quad \frac{\partial N_I(\xi, \eta)}{\partial \xi} z_I \right)^T \quad (39)$$

$$\mathbf{g}_\eta = \left(\frac{\partial N_I(\xi, \eta)}{\partial \eta} x_I \quad \frac{\partial N_I(\xi, \eta)}{\partial \eta} y_I \quad \frac{\partial N_I(\xi, \eta)}{\partial \eta} z_I \right)^T \quad (40)$$

the normal to the mid-surface can be computed as

$$\mathbf{n} = \frac{\mathbf{g}_\xi \times \mathbf{g}_\eta}{\|\mathbf{g}_\xi \times \mathbf{g}_\eta\|} \quad (41)$$

It should be noted that the current configuration Jacobian depends on the value of the final thickness, while the deformation of the membrane mid-surface is not sufficient for evaluating the thickness stretch.

The plane stress assumption ($\sigma_{33} = 0$) provides an extra condition which relates the thickness variation with the in-plane strain. Assuming constant thickness when computing the current configuration, the Jacobian \mathbf{J} is clearly erroneous. It has been shown [29] that this error can be avoided by ensuring that the stresses are not affected by spurious out-of-plane stretches. This can be done by choosing an appropriate form for the elasticity tensor. For membranes initially lying in the x-y plane, an elasticity tensor in the form

$$\mathbf{D} = \frac{E}{1 - \nu^2} \begin{pmatrix} 1 & \nu & 0 & 0 & 0 & 0 \\ \nu & 1 & 0 & 0 & 0 & 0 \\ 0 & 0 & 0 & 0 & 0 & 0 \\ 0 & 0 & 0 & \frac{1-\nu}{2} & 0 & 0 \\ 0 & 0 & 0 & 0 & 0 & 0 \\ 0 & 0 & 0 & 0 & 0 & 0 \end{pmatrix} \quad (42)$$

ensures that all the out-of-plane strains are multiplied by zero (note that the non-zero terms exactly reproduce the components of the plane stress isotropic elasticity tensor).

In order to deal with an arbitrary initial configuration of the membrane (i.e. not necessarily coinciding with x-y plane), one must define the above elasticity tensor in the local system of coordinates and then bring it back to the global system of coordinates via a coordinate transformation. The tangent system of coordinates can be written as

$$\mathbf{v}_1 = \frac{\mathbf{g}_\xi}{\|\mathbf{g}_\xi\|} ; \quad \mathbf{v}_2 = \frac{\mathbf{n} \times \mathbf{v}_1}{\|\mathbf{n} \times \mathbf{v}_1\|} ; \quad \mathbf{v}_3 = \mathbf{n} \quad (43)$$

The corresponding local-to-global rotation matrix can be written as:

$$\mathbf{T} = \begin{pmatrix} a_{11}^2 & a_{21}^2 & a_{31}^2 & 2a_{22}a_{12} & 2a_{32}a_{22} & 2a_{32}a_{12} \\ a_{12}^2 & a_{22}^2 & a_{32}^2 & 2a_{22}a_{12} & 2a_{32}a_{22} & 2a_{32}a_{12} \\ a_{13}^2 & a_{23}^2 & a_{33}^2 & 2a_{23}a_{13} & 2a_{33}a_{23} & 2a_{33}a_{13} \\ a_{11}a_{12} & a_{21}a_{22} & a_{31}a_{32} & a_{21}a_{12} + a_{11}a_{22} & a_{31}a_{22} + a_{21}a_{32} & a_{31}a_{12} + a_{11}a_{32} \\ a_{12}a_{13} & a_{22}a_{23} & a_{32}a_{33} & a_{22}a_{13} + a_{12}a_{23} & a_{32}a_{23} + a_{22}a_{33} & a_{32}a_{13} + a_{12}a_{33} \\ a_{13}a_{11} & a_{23}a_{21} & a_{33}a_{31} & a_{21}a_{13} + a_{11}a_{23} & a_{31}a_{23} + a_{21}a_{33} & a_{31}a_{13} + a_{11}a_{33} \end{pmatrix} \quad (44)$$

where $a_{ij} = \mathbf{v}_i \cdot \mathbf{e}_j$

Thus the effective elasticity tensor in global coordinates reads

$$\mathbf{D}_e = \mathbf{T}^T \mathbf{D} \mathbf{T} \quad (45)$$

Having introduced the above constitutive law, the membrane can be implemented as a standard 3D total Lagrangian element.

The discrete form of the momentum residual (Eq. 4) can be written as:

$$\bar{\mathbf{r}}_m^s = \mathbf{f}_{ext} - \mathbf{M} \frac{\mathbf{d}_{n+1} - \mathbf{d}_n - \mathbf{v}_n \Delta t}{\Delta t^2} - \mathbf{f}_{int} \quad (46)$$

where \mathbf{f}_{int} is defined as

$$\mathbf{f}_{int} = \int_{\Omega_0} \mathbf{B}_0^T \mathbf{P} d\Omega_0 \quad (47)$$

where total Lagrangian strain-displacement matrix \mathbf{B}_0 is defined as:

$$\mathbf{B}_{0I} = \begin{pmatrix} \frac{\partial N_I}{\partial X} \frac{\partial x}{\partial X} & \frac{\partial N_I}{\partial X} \frac{\partial y}{\partial X} & \frac{\partial N_I}{\partial X} \frac{\partial z}{\partial X} \\ \frac{\partial N_I}{\partial Y} \frac{\partial x}{\partial Y} & \frac{\partial N_I}{\partial Y} \frac{\partial y}{\partial Y} & \frac{\partial N_I}{\partial Y} \frac{\partial z}{\partial Y} \\ \frac{\partial N_I}{\partial Z} \frac{\partial x}{\partial Z} & \frac{\partial N_I}{\partial Z} \frac{\partial y}{\partial Z} & \frac{\partial N_I}{\partial Z} \frac{\partial z}{\partial Z} \\ \frac{\partial N_I}{\partial Y} \frac{\partial x}{\partial Z} + \frac{\partial N_I}{\partial Z} \frac{\partial x}{\partial Y} & \frac{\partial N_I}{\partial Y} \frac{\partial y}{\partial Z} + \frac{\partial N_I}{\partial Z} \frac{\partial y}{\partial Y} & \frac{\partial N_I}{\partial Y} \frac{\partial z}{\partial Z} + \frac{\partial N_I}{\partial Z} \frac{\partial z}{\partial Y} \\ \frac{\partial N_I}{\partial X} \frac{\partial x}{\partial Z} + \frac{\partial N_I}{\partial Z} \frac{\partial x}{\partial X} & \frac{\partial N_I}{\partial X} \frac{\partial y}{\partial Z} + \frac{\partial N_I}{\partial Z} \frac{\partial y}{\partial X} & \frac{\partial N_I}{\partial X} \frac{\partial z}{\partial Z} + \frac{\partial N_I}{\partial Z} \frac{\partial z}{\partial X} \\ \frac{\partial N_I}{\partial X} \frac{\partial x}{\partial Y} + \frac{\partial N_I}{\partial Y} \frac{\partial x}{\partial X} & \frac{\partial N_I}{\partial X} \frac{\partial y}{\partial Y} + \frac{\partial N_I}{\partial Y} \frac{\partial y}{\partial X} & \frac{\partial N_I}{\partial X} \frac{\partial z}{\partial Y} + \frac{\partial N_I}{\partial Y} \frac{\partial z}{\partial X} \end{pmatrix} \quad (48)$$

In order to compute \mathbf{f}_{int} the following steps are carried out:

1. Compute the strain-displacement matrix \mathbf{B}_0 (Eq. 48)
2. Compute the deformation gradient $\mathbf{F} = \mathbf{I} + \sum_I \mathbf{B}_{0I} \mathbf{d}_I$
3. Compute the Green-Lagrange strain tensor as $\mathbf{E} = \frac{1}{2} (\mathbf{F}^T \mathbf{F} - \mathbf{I})$
4. Compute the second Piola-Kirchhoff stress \mathbf{S} using the constitutive relation $\mathbf{S} = \mathbf{D}_e \mathbf{E}$
5. Compute the nominal stress tensor $\mathbf{P} = \mathbf{S} \mathbf{F}^T$

$$\mathbf{F} = \frac{\partial \mathbf{d}}{\partial \mathbf{X}} + \mathbf{I} \quad (49)$$

According to [30], the linearization of Eq. (46) with respect to displacement results in the following tangent stiffness matrix:

$$\mathbf{H}^s = \mathbf{M} + \mathbf{K}_g + \mathbf{K}_m \quad (50)$$

where the geometric (\mathbf{K}_g) and material (\mathbf{K}_m) stiffness matrices are defined as

$$\mathbf{K}_g = \int_{\Omega_e} \left[\frac{\partial \mathbf{N}}{\partial \mathbf{X}} \right]^T \mathbf{S} \left[\frac{\partial \mathbf{N}}{\partial \mathbf{X}} \right] d\Omega_e \quad (51)$$

$$\mathbf{K}_m = \int_{\Omega_e} \mathbf{B}_0^T \mathbf{D}_e \mathbf{B}_0 d\Omega_e \quad (52)$$

The shape function derivatives are computed as

$$\left[\frac{\partial \mathbf{N}}{\partial \mathbf{X}} \right] = \left[\frac{\partial \mathbf{N}}{\partial \boldsymbol{\xi}} \right] \mathbf{J}_0^{-1} \quad (53)$$

Internal fluid. In order to define a monolithic system for the internal fluid and the membrane sharing the same nodal variables we use an updated Lagrangian displacement-based fluid formulation that can be naturally coupled to a displacement-based membrane element. This type of fluid formulations for a general FSI problem was originally proposed in [14].

A displacement-based FEM model for the fluid is obtained by rewriting the governing equations (Eqs. (1),(2)) in terms of displacements as:

$$\rho \frac{D^2 \mathbf{d}}{Dt^2} - \mu \Delta \left(\frac{D\mathbf{d}}{Dt} \right) + \nabla p = \mathbf{f} \quad (54)$$

$$\frac{\partial p}{\partial t} = -\kappa \nabla \cdot \frac{D\mathbf{d}}{Dt} \quad (55)$$

Linear interpolations for the displacements and the pressure over 4-noded tetrahedra are used for the spatial discretization as:

$$\mathbf{d}(\mathbf{X}, t) = \sum_{I=1}^4 \bar{\mathbf{d}}_I(t) \mathbf{N}_I(\mathbf{X}) \quad (56)$$

$$p(\mathbf{X}, t) = \sum_{I=1}^4 \bar{p}_I(t) N_I(\mathbf{X}) \quad (57)$$

The time approximation follows a Backward Euler scheme, i.e.

$$\bar{\mathbf{d}}_{n+1} = \bar{\mathbf{v}}_{n+1} \Delta t \quad (58)$$

$$\bar{\mathbf{v}}_{n+1} = \bar{\mathbf{v}}_n + \bar{\mathbf{a}}_{n+1} \Delta t \quad (59)$$

Thus,

$$\frac{D\bar{\mathbf{d}}}{Dt} = \bar{\mathbf{v}}_{n+1} = \frac{\bar{\mathbf{d}}_{n+1}}{\Delta t} \quad (60)$$

$$\frac{D^2 \bar{\mathbf{d}}}{Dt^2} = \bar{\mathbf{a}}_{n+1} = \frac{\bar{\mathbf{d}}_{n+1}}{\Delta t^2} - \frac{\bar{\mathbf{v}}_n}{\Delta t} \quad (61)$$

where $\bar{\mathbf{v}}$ and $\bar{\mathbf{a}}$ are the velocity and the acceleration vectors, respectively defined in the Lagrangian framework (i.e. excluding the convection terms).

Given $\bar{\mathbf{d}}_n$ and $\bar{\mathbf{p}}_n$ at t_n , the discrete problem consists in finding $\bar{\mathbf{d}}_{n+1}$ and $\bar{\mathbf{p}}_{n+1}$ at t_{n+1} as the solution of

$$\bar{\mathbf{r}}_m^{fi} = 0 \quad (62)$$

$$\bar{\mathbf{r}}_c^{fi} = 0 \quad (63)$$

where $\bar{\mathbf{r}}_m^{fi}$ and $\bar{\mathbf{r}}_c^{fi}$ are the residua of the momentum and continuity equations, defined as:

$$\bar{\mathbf{r}}_m^{fi} = \mathbf{F} - \rho \mathbf{M} \left(\frac{\bar{\mathbf{d}}_{n+1}}{\Delta t^2} - \frac{\bar{\mathbf{v}}_n}{\Delta t} \right) + \mu \mathbf{L} \frac{\bar{\mathbf{d}}_{n+1}}{\Delta t} - \mathbf{G} \bar{\mathbf{p}}_{n+1} \quad (64)$$

$$\bar{\mathbf{r}}_c^{fi} = \kappa \mathbf{D} \bar{\mathbf{d}}_{n+1} - \mathbf{M}_p (\bar{\mathbf{p}}_{n+1} - \bar{\mathbf{p}}_n) \quad (65)$$

where \mathbf{M} , \mathbf{L} , \mathbf{G} and \mathbf{D} are mass, Laplacian, gradient and divergence matrices, respectively. The pressure mass matrix is distinguished by the "p" subscript. $\bar{\mathbf{v}}$ and $\bar{\mathbf{p}}$ are the nodal velocity and the nodal pressure vectors, respectively and \mathbf{f}_{ext} is the body force vector.

The discrete operators follow the definitions given by Eqs. (23)-(29), but are now calculated using the current configuration \mathbf{X}_{n+1} , according to the standard updated Lagrangian approach.

In order to define a monolithic model for the internal fluid and the membrane, the fluid formulation should have the same degrees of freedom as the structural one. This can be done by approximating the pressure increment to be used in the linearization of the momentum equation Eq. (21) leading to [31]:

$$\mathbf{G} \bar{\mathbf{p}}_{n+1} = \mathbf{G} (\bar{\mathbf{p}}_n + \delta \bar{\mathbf{p}}) \approx \mathbf{G} \bar{\mathbf{p}}_n + \left[\sum_{elem} \int_{\Omega_e} \mathbf{B}^T \mathbf{C}_K \mathbf{B} d\Omega_e \right] \bar{\mathbf{d}}_{n+1} \quad (66)$$

where

$$\mathbf{B}_I = \begin{pmatrix} \frac{\partial N_I}{\partial x} & 0 & 0 \\ 0 & \frac{\partial N_I}{\partial y} & 0 \\ 0 & 0 & \frac{\partial N_I}{\partial z} \\ \frac{\partial N_I}{\partial x} & \frac{\partial N_I}{\partial y} & \frac{\partial N_I}{\partial z} \\ \frac{\partial N_I}{\partial y} & 0 & 0 \\ \frac{\partial N_I}{\partial z} & 0 & 0 \\ 0 & \frac{\partial N_I}{\partial z} & \frac{\partial N_I}{\partial y} \end{pmatrix} \quad (67) \quad \mathbf{C}_K = \begin{pmatrix} \kappa & \kappa & \kappa & 0 & 0 & 0 \\ \kappa & \kappa & \kappa & 0 & 0 & 0 \\ \kappa & \kappa & \kappa & 0 & 0 & 0 \\ 0 & 0 & 0 & 0 & 0 & 0 \\ 0 & 0 & 0 & 0 & 0 & 0 \\ 0 & 0 & 0 & 0 & 0 & 0 \end{pmatrix} \quad (68)$$

The linearization of the pressure gradient with respect to the displacements can thus be expressed as:

$$\frac{\partial \mathbf{G} \bar{\mathbf{p}}}{\partial \bar{\mathbf{d}}} \approx \sum_{elem} \int_{\Omega_e} \mathbf{B}^T \mathbf{C}_K \mathbf{B} d\Omega_e \quad (69)$$

The tangent matrix of the momentum equation reads

$$\mathbf{H}^{fi} = \frac{\partial \bar{\mathbf{r}}_m}{\partial \bar{\mathbf{d}}} = \frac{\mathbf{M}}{\Delta t^2} + \frac{\mu \mathbf{L}}{\Delta t} + \sum_{elem} \int_{\Omega_e} \mathbf{B}^T \mathbf{C}_K \mathbf{B} d\Omega_e \quad (70)$$

Identically to what has been done for pressure stabilization in the external fluid domain, the continuity equation Eq. (65) as:

$$\bar{\mathbf{r}}_c = \kappa \mathbf{D} \bar{\mathbf{d}}_{n+1} - \left(\mathbf{M}_p^l \bar{\mathbf{p}}_{n+1} - \mathbf{M}_p^c \bar{\mathbf{p}}_n \right) \quad (71)$$

Monolithic membrane-internal fluid system. Eqs. (64), (46), (70), (50) define the residua and tangent matrices of the internal fluid and the membrane elements. All are written in terms of nodal displacements. Thus, the membrane-fluid system can be solved monolithically using a single mesh and assembling a global system by the standard finite element procedure following the strategy proposed for a general fluid-structure problem in [14].

In order to account for the effect of the external fluid the following Neumann term is added to the momentum equation residual $\bar{\mathbf{r}}_{mon}$:

$$\bar{\mathbf{F}}_N = - \int_{\Omega^s} \mathbf{N} \bar{\mathbf{p}}_{n+1}^{fe} \cdot \mathbf{n} d\Omega^s + \mu^{fe} \int_{\Omega^s} \left[\nabla \left(\mathbf{N} \mathbf{v}_{n+1}^{fe} \right) + \nabla \left(\mathbf{N} \mathbf{v}_{n+1}^{fe} \right)^T \right] \cdot \mathbf{n} d\Omega^s + \mu^{fe} \int_{\Omega^s} \left[\nabla \left(\mathbf{N} \mathbf{v}_{n+1}^{fe} \right) + \nabla \left(\mathbf{N} \mathbf{v}_{n+1}^{fe} \right)^T \right] \cdot \mathbf{m} d\Omega^s \quad (72)$$

The integrands (pressure and viscous stresses) are computed in Ω^{fe} and then are projected onto Ω_s , where the integrals are computed.

The monolithic solution can be expressed in an algorithmic form shown in Table 1:

- | |
|--|
| <ol style="list-style-type: none"> 1. Discretize the internal fluid-membrane domain by a single Lagrangian mesh 2. Assemble the monolithic residual $\bar{\mathbf{r}}_{mon}$ by looping over the elements: <ul style="list-style-type: none"> If fluid element: use Eq. (64) If solid element: use Eq. (46) Add the Neumann term (representing external fluid pressure and shear stress) defined by Eq. (72) to $\bar{\mathbf{r}}_{mon}$ 3. Assemble the monolithic tangent matrix \mathbf{H}_{mon} by looping over the elements: <ul style="list-style-type: none"> If fluid element: use Eq. (70) If solid element: use Eq. (50) 4. Solve the non-linear monolithic momentum equation $\mathbf{H}_{mon} \delta \bar{\mathbf{d}} = \bar{\mathbf{r}}_{mon}$ using Newton-Raphson procedure and update the nodal displacements as $\bar{\mathbf{d}}_{n+1}^{i+1} = \bar{\mathbf{d}}_{n+1}^i + \delta \bar{\mathbf{d}}$ at each non-linear iteration. 5. Update the fluid pressure using Eq. (71). 6. Re-mesh the fluid domain Ω^{fi}. 7. Go to next time step and repeat from step 2 |
|--|

Table 1: Monolithic solution algorithm for the domain consisting of a membrane filled with an internal fluid.

3.3. Solution strategy for analysis of filled membranes interacting with an external fluid

To this end the discrete governing systems describing an external fluid (Eulerian) and a membrane filled in with an internal fluid (Lagrangian) have been specified. We will consider now the case when the filled membrane interacts with

the external fluid. Let us consider that at the time step t_n the solution (displacement $\bar{\mathbf{d}}_n$, velocity $\bar{\mathbf{v}}_n$ and pressure $\bar{\mathbf{p}}_n$) is known in both the domains $\Omega_r^{Eul} = \Omega^{fe}$ (external fluid) and $\Omega^{Lag} = \Omega^s \cup \Omega^{fi}$. To find the displacement/velocity and pressure fields at t_{n+1} the algorithm shown in Table 2 is implemented:

1. Solve the internal fluid-membrane problem using a monolithic Lagrangian model using the algorithm specified in Table 1.
Output: new position of the Lagrangian mesh, $\bar{\mathbf{d}}_{n+1}$, $\bar{\mathbf{p}}_{n+1}$ in $\Omega^{Lag} = \Omega^{fi} \cup \Omega^s$.
2. Identify the position of the Lagrangian domain within the Eulerian one. Identify the "real Eulerian fluid" and the "fictitious subdomain" (the one composed by the elements fully enclosed by the membrane).
Output: Γ_I within the fixed Eulerian mesh, Ω^{fe} .
3. "Switch off" the fictitious elements
4. Solve the external fluid problem in Ω^{fe} (Eq. (31)) equipped with the interface Dirichlet boundary condition defined by Eq. (33) representing the velocity of the Lagrangian domain in the Eulerian mesh. Output: velocity and pressure $\bar{\mathbf{v}}_{n+1}$ and $\bar{\mathbf{p}}_{n+1}$ in Ω^{fe} .
5. Project the external fluid pressure and the viscous stresses from Ω^{fe} onto the membrane Ω^s and add the corresponding Neumann term (Eq. (72)) term to the monolithic Lagrangian momentum equation at the next time step:
6. Go to next time step

Table 2: Solution algorithm for the domain consisting of a closed membrane filled with an internal fluid immersed in an external fluid.

Step 1 involves finding the intersection between the Lagrangian surface mesh and the Eulerian elements. This is implemented using an oct-tree search for ensuring computational efficiency according. A polygon defined by these intersections provides the representation of the Lagrangian surface within the Eulerian mesh, i.e. the interface Γ_I . In Step 2 the elements that lie fully inside the closure defined by Γ_I are marked as "fictitious" and the ones that lie fully outside as "real". The elements that are intersected by Γ_I are the interface elements that contain both the real and the fictitious nodes. The fictitious nodes of the interface elements are used to impose the interface Dirichlet boundary condition resulting from solving (Eq. (33)). This equation takes into account the location of the intersection (see [27] for the way this equation can be solved).

4. Examples

In this section several numerical examples are solved. The formulation previously described has been implemented within Kratos Multiphysics, an Open

Source C++ object oriented Finite Element framework [32]. The Newton-Raphson method was used to solve the governing system of equations. At every non-linear iteration, the linear system representing the Lagrangian domain (membrane+fluid) was solved using the conjugate gradient (CG) method, while a stabilized Bi-conjugate gradient method (BICGSTAB) was applied in the Eulerian domain (since in this case the linear system is not symmetric). The convergence criteria used is as follows:

- non-linear iterations tolerances
 - Velocity. Relative: $\epsilon_v = \frac{\|\delta \mathbf{v}\|}{\|\mathbf{v}_{n+1}\|} < 10^{-6}$. Absolute: 10^{-8}
 - Pressure. Relative: $\epsilon_p = \frac{\|\delta p\|}{\|p_{n+1}\|} < 10^{-4}$. Absolute: 10^{-6}
 - Displacement. Relative: $\epsilon_d = \frac{\|\delta \mathbf{d}\|}{\|\mathbf{d}_{n+1}\|} < 10^{-6}$. Absolute: 10^{-8}
- linear solver tolerances
 - CG: 10^{-8}
 - BICGSTAB: 10^{-8}

The results presented in the examples below were obtained using a staggered version of the Eulerian-Lagrangian coupling strategy if not mentioned otherwise².

In the examples below the bulk modulus of the fluid is set to $\kappa = 10^7$ Pa if not mentioned otherwise. This value ensures accurate approximation of an incompressible behavior for the problems considered, while leading to stable pressure results. We note that using the physical value of water bulk modulus would result in pressure instabilities when applying the quasi-incompressible approach used in the present work.

4.1. Inflation of a square airbag

The aim of the first example is to validate the structural model. The example (proposed in [33] and used for validation purposes in [11]) models an airbag inflated by an internal pressure of 24 Pa. The edge length of the bag is 0.3048 m and the material thickness is 0.00003048 m. The elastic modulus is 206.8 MPa, the Poisson's ratio $\nu = 0.3$. Self weight of the structure is not considered. Symmetry conditions enable modeling the actual bag (made of two

²We note that the Eulerian-Lagrangian coupling in this work is implemented with a possibility of executing an iterative coupling. In order to obtain a tight coupling between the Eulerian and the Lagrangian models, Steps 3 and 4 of the algorithm presented in Table 2 are iterated until convergence in terms of relative incremental displacement of the membrane is obtained. Nevertheless, Examples 1 and 2 solved below do not involve external fluid, Example 3 a) is characterized by a static solution. For Example 3 b) analytical solution is known and the staggered model provided a stable and accurate result. In Example 4 both staggered and iterative solutions were tested leading to nearly identical results.

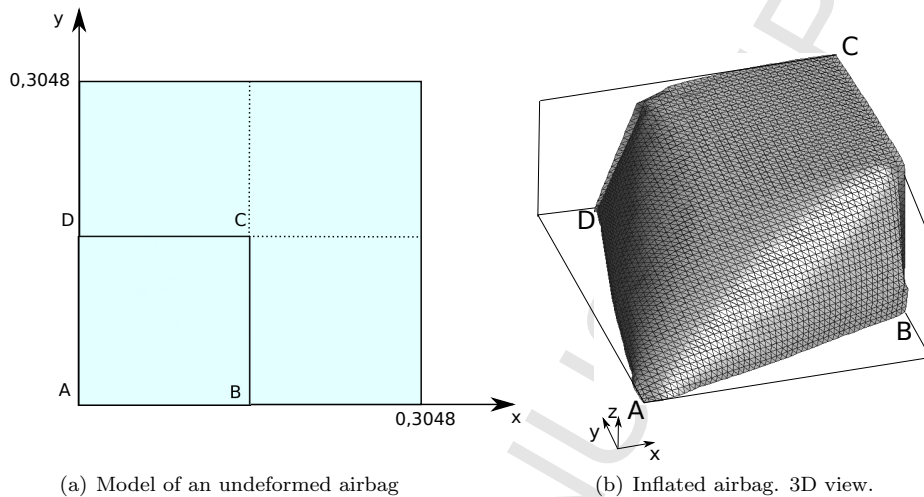


Figure 5: Inflated airbag example

square surfaces sewn along four edges) by considering one fourth of one of the airbag surfaces. The initial geometry is shown in Fig. 5(a).

The symmetry boundary conditions are as follows:

- Fixed the off-plane (z) displacements at the edges AB and AD
- Fixed horizontal (x) displacements at edge BC
- Fixed vertical (y) displacements at edge DC

The simulations have been carried out using structured meshes of 3-noded triangles. The results shown below correspond to the mesh corresponding to 50 partitions per edge (element size of 0.003 m). Convergence analysis (not reproduced here) with respect to mesh size confirmed that this mesh resolution is sufficient for obtaining accurate results. A 3D view of the equilibrium configuration of the inflated airbag obtained using the present model is shown in Fig. 5(b). The vertical displacement of point C at equilibrium was estimated as 0.072 m. The depth of maximum indents (i.e. horizontal component of the vector AD and vertical component of the vector AB in the deformed configuration) is equal to 0.04 m. In reference [33] the Z (off-plane) displacement of point C at equilibrium was estimated as 0.075 m and the depth of the indentations as 0.04 m.

In order to facilitate the comparison with [11], the results of the present simulation were superimposed with the data from the mentioned paper (see Fig. 6). The simulation in [11] was done considering the entire domain, while the present simulation considered only a quarter due to symmetry. Our results are shown in the left lower quadrant of the figure. One can see a good overall

Point	Present work	[33]	[11]
C	0.072	0.075	<i>N/A</i>
B	0.04	0.04	0.035
D	0.04	0.04	0.035

Table 3: Inflated airbag example. Displacements at different points (comparisons with [33] and [11]).

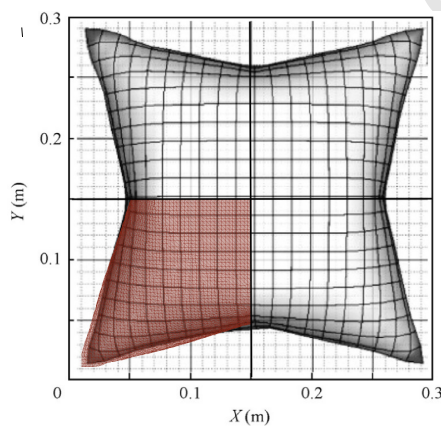


Figure 6: Inflated airbag example (xy-plane). Comparison with [11].

agreement. However, the membrane stretching observed in the present simulation is slightly larger. In [11] the indentation depth was estimated as ≈ 0.35 m, which is slightly lower than the value obtained in the present work and in [33] (≈ 0.04). No off-plane displacement can be read from the graph provided in [11]. However, the authors claim that a value similar to the one computed in [33] was obtained.

The comparisons of displacements at various points is summarized in Table 3

We note that in order to obtain a stable solution it was necessary to introduce damping into the present model. Otherwise instabilities in the locations where the membrane was undergoing compression were observed.

4.2. Hanging water bag

The example proposed in [34] models a hanging water bag partially filled with liquid. In the reference the problem was modeled using axisymmetric shell elements. Water action was modeled by applying the corresponding pressure (i.e. no fluid simulation was actually performed). The schematic representation of the test is shown in Fig. 7.

The properties of the bag are as follows: elastic isotropic material with Young's modulus of 0.1 GPa, Poisson's ratio is equal to 0.2, density is 1000

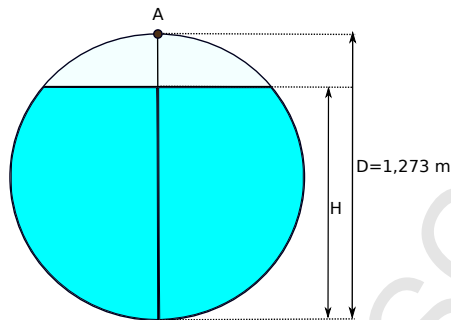


Figure 7: Hanging water-bag model. Initial (undeformed) configuration.

kg/m^3 . The thickness of the bag is 1 mm. The unstrained configuration of the bag is circular with a radius of 0.63662 m. Initial water height H is 0.837 (which corresponds to the filling ratio of 0.7 indicated in [34]). Point A is fixed. In the present work, water was modeled as a fluid with density of $1000 kg/m^3$ and viscosity of $10^{-6} m^2/s$. Due to symmetry, only a quarter of the domain is simulated using a mesh of 7000 3-noded triangles for the membrane and 250000 4-noded tetrahedra for the fluid. Fig. 8(a) shows the deformed configuration of the bag as well as the pressure distribution. The maximum pressure of the fluid ≈ 12000 Pa is obtained at the bottom of the bag. The membrane loading can be seen in Fig. 8(b), where the distribution of the first principal PK2 stress is shown. The bottom-most region of the membrane undergoes a load of 4 MPa, while at the top (pinning point) the stress around 90 MPa is observed. The largest stress is observed in the "neck" region of the water bag, i.e. the part not filled with water. There the stress grows from 5 MPa to 90 MPa.

Comparison with the results obtained in [34] is shown Fig. 8(c). The dashed line corresponds to the reference solution, while the solid line indicates the result provided by the present model. One can see that the maximum vertical length of 1.65 m is obtained in the present simulation (1.7 in [34]). Maximum width of 0.5 m is observed. The free surface location obtained in the present method coincides with the result of [34]. The volume of the fluid in the original (undeformed) and final (equilibrium) configuration was computed: $V_0 = 0.21 m^3$, $V_{eq} = 0.206 m^3$, which indicates the good mass conservation features of the present model.

4.3. Pinned balloon under water

In this example, a balloon filled with an internal fluid is immersed into an external fluid. The balloon is pinned at its bottom-most point. The example is solved in order to assess the capability of the model for representing a discontinuity of the pressure and the pressure gradient across the membrane wall. A scheme of the example is shown in Fig. 9. The geometry of the problem is as follows: water height $H=0.4$ m, container width $D=0.2$ m, depth of the balloon

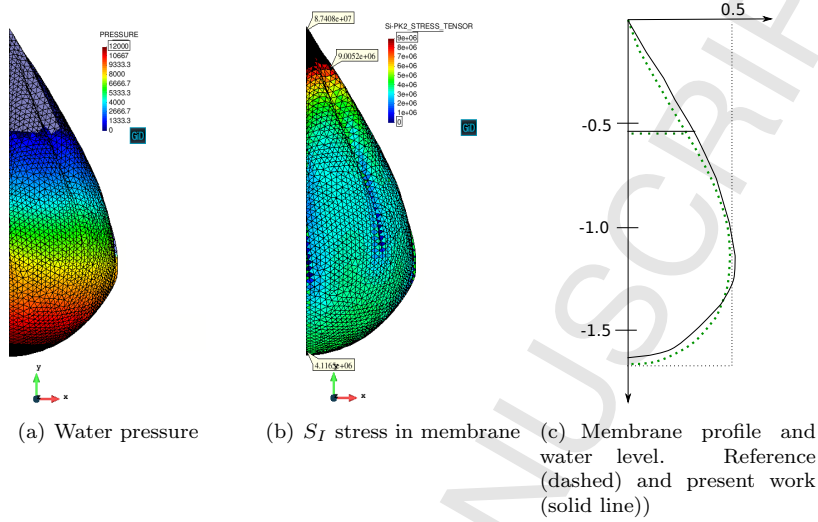


Figure 8: Hanging water bag. Equilibrium configuration

center $h=0.3$ m, balloon radius $r=0.05$ m. The density of the external fluid is $\rho_1 = 1000 \text{ kg/m}^3$. **Viscosity of $10^{-4} \text{ m}^2/\text{s}$ were used in both fluids.**

Two densities of the internal fluid are considered: $\rho_2 = 100 \text{ kg/m}^3$ and $\rho_2 = 10 \text{ kg/m}^3$. The equilibrium configuration for both cases is shown in Fig. 10. One can see that the equilibrium configurations are identical, which is an expected result provided that the fluids are nearly incompressible and material stretching due to buoyancy is negligible.

Fig. 11 displays the pressure distribution along the vertical cut made at the center (symmetry axis) of the domain. The hydrostatic pressure varies from 3920 Pa at the bottom of the external fluid domain to 0 Pa at the free surface. At $y=0.05$ m the pinned membrane is located. This corresponds to the location of the first discontinuity both in pressure and its gradient. While in the case of internal fluid density of 100 kg/m^3 (Fig. 11(a)) one can distinguish a slope in the range corresponding to the internal fluid, in case of internal fluid density of 10 kg/m^3 (Fig. 11(b)), the slope is nearly horizontal. A pressure jump at the top most point of the membrane of approximately 810 and 890 Pa is observed for the two respective cases.

4.4. Rising balloon

Next, a transient case is analyzed. The geometry of the problem is adopted from the previous example (see Fig. 9). The boundary conditions are different: now the balloon is not pinned, but is let free to rise due to buoyancy. Density of the external and the internal fluids are $\rho_1 = 1000 \text{ kg/m}^3$ and $\rho_2 = 100 \text{ kg/m}^3$, respectively.

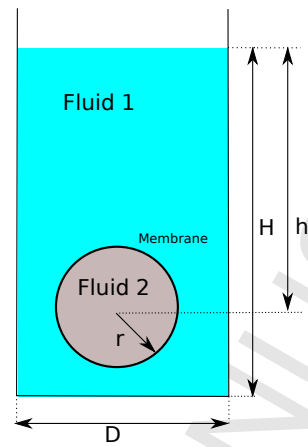


Figure 9: A scheme of the underwater balloon example.

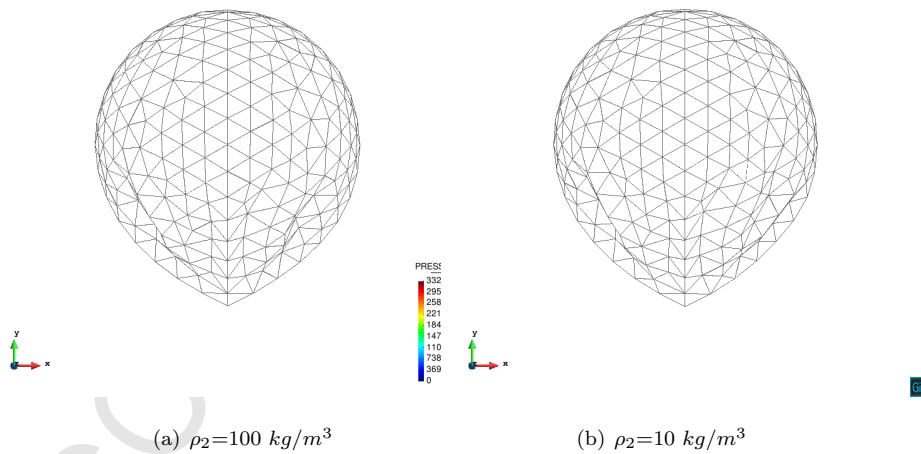


Figure 10: Pinned underwater balloon. Equilibrium configuration.

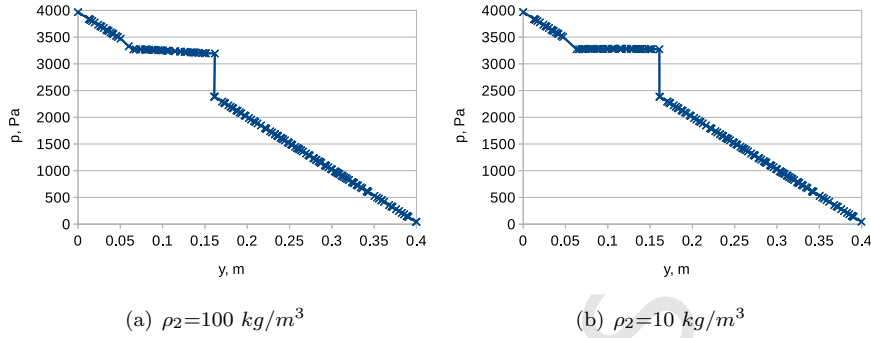


Figure 11: Pinned balloon. Pressure at equilibrium along the vertical symmetry axis.

In order to be able to compare the simulation results with an analytic solution, a high fluid viscosity is chosen: $\nu_1 = \nu_2 = 10^{-2} \text{ Pa}\cdot\text{s}$ (leading to a Reynold's number $Re \approx 2, 5$). The membrane properties are: density $\rho_m = 1000 \text{ kg/m}^3$, Young's modulus $E = 1 \text{ MPa}$, Poisson's ratio $\nu = 0.1$, thickness $t = 0.0001 \text{ m}$.

Fig. 12 shows the simulation results at different time instances. One can see the Lagrangian domain (consisting of a membrane and the internal fluid) and its representation within the fixed Eulerian mesh. The vertical velocity distribution is shown in a cut in the middle of the domain along the x-y plane.

Since the chosen settings ensure a laminar flow regime, the transient velocity can be estimated by an analytic solution, given by

$$v(t) = v_t e^{-bt/m} \quad (73)$$

where $v_t = \frac{(\rho_1 - \rho_2)Vg}{b}$ is the terminal velocity, $b = 6\pi\rho_1\nu_1 r$ is the laminar drag constant and m is the mass of the filled balloon. The membrane mass is nearly negligible here. Substituting the numerical values one obtains:

$$v(t) = 0.47e^{-9.42t/0.52} \quad (74)$$

Fig. 13(a) compares the analytic solution with the simulation result. One can see a nearly perfect match between the graphs. However, slight oscillations are observed in the simulation results due to membrane "breathing modes" that are not fully damped. Fig. 13(b) displays the effect of increasing the viscosity of the inner fluid: one can see that when increasing the viscosity of the internal fluid to $1 \text{ Pa}\cdot\text{s}$, the oscillatory behavior vanishes.

4.5. Water-bag offshore reefs for coastal protection

The aim of this example is to assess the applicability of the proposed model to a practical civil engineering problem. The problem consists in modeling the effect of immersed water-bag reefs on the height of the sea waves. First, we briefly introduce the context of the problem.

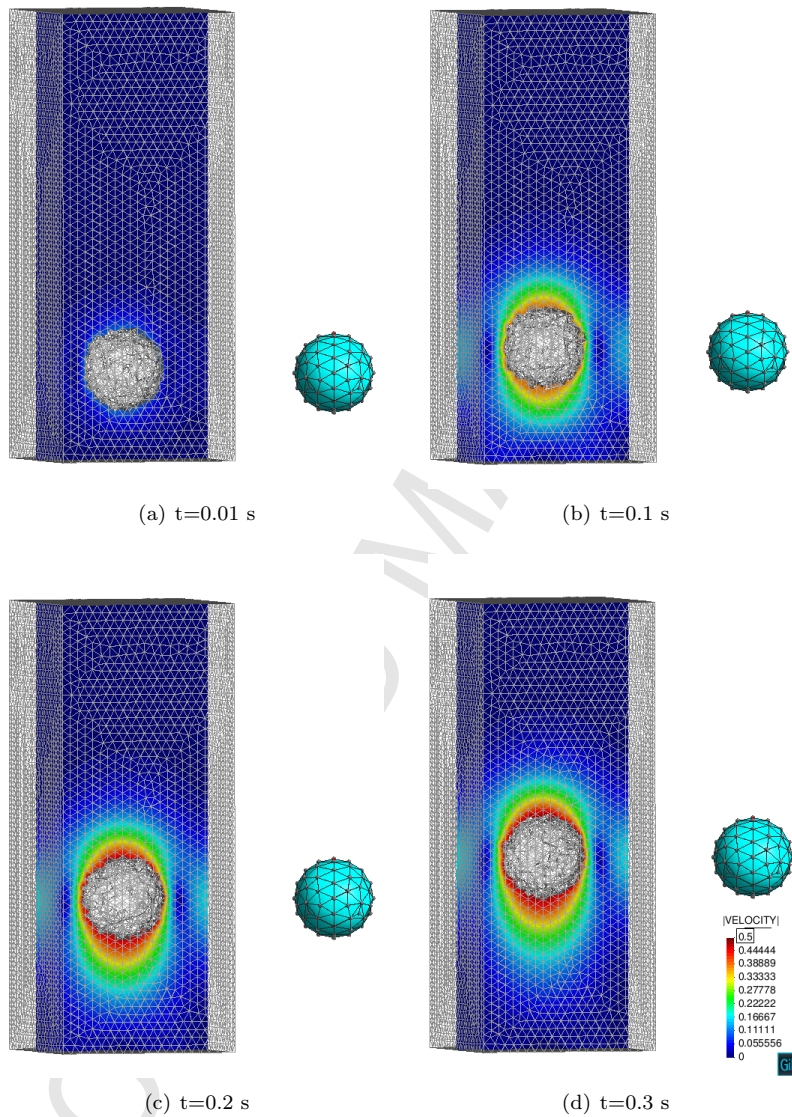
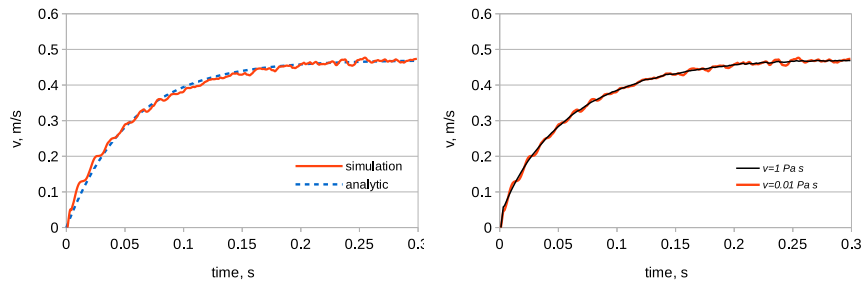


Figure 12: Rising balloon. Eulerian and Lagrangian domains at various time instances



(a) Comparison with the analytic solution. (b) Effect of the internal fluid viscosity

Figure 13: Evolution of the rising balloon's vertical velocity.

In order to diminish the damage caused by the sea waves to sand beaches, concrete offshore reefs are often installed in the direction parallel to the coast-line [35], [36]. The main goal of such structures is to slow-down the sedimentary erosion process via diminishing the wave energy in the vicinity of the coast. Three mechanisms are generally involved: partial reflection of the wave by the reef, incident transmission above the crest of the structure and diffraction of the wave (around the reef - at the lateral sides, or through the reef in case of non-zero permeability). Out of the latter two mechanisms, for the reefs with the crests above the sea level, diffraction is the predominant mode, while for fully submerged impermeable reefs, it becomes nearly negligible. For aesthetic and security reasons, the submerged reefs may be a preferable design solution.

Taking into account the wave energy $E \sim H^2$, where H is the wave height for assessing the effect of the reef quantitatively, the coefficient of transmission is defined as

$$K_t = \frac{H_t}{H_i} \quad (75)$$

where H_i is the average incident wave height, while H_t is the transmitted wave height (i.e. after passing the reef - see a scheme in Fig. 14).

An alternative to the standard reefs made of concrete blocks is the use of submerged flexible structures. In this work we present a first assessment of the possibility of using a submerged reef made of membrane bags filled with water.

Such design would not only diminish the reef construction cost, but would also offer an ambient-friendly solution. In order to design and assess the functionality of such flexible submerged structures, numerical simulation using the methodology proposed in this paper can be very beneficial.

The example presented below shows a hypothetical case of free-surface flow interacting with a submerged flexible reef in order to assess its transmission effect. A schematic of the test is displayed in Fig. 15. A water channel of 40 m length, 3 m width and 5 m height is filled with water up to 2.5 m. At

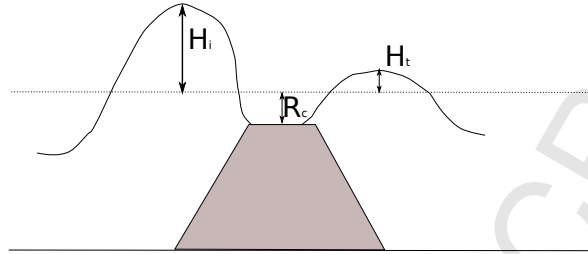


Figure 14: Influence of the reef upon the wave height.

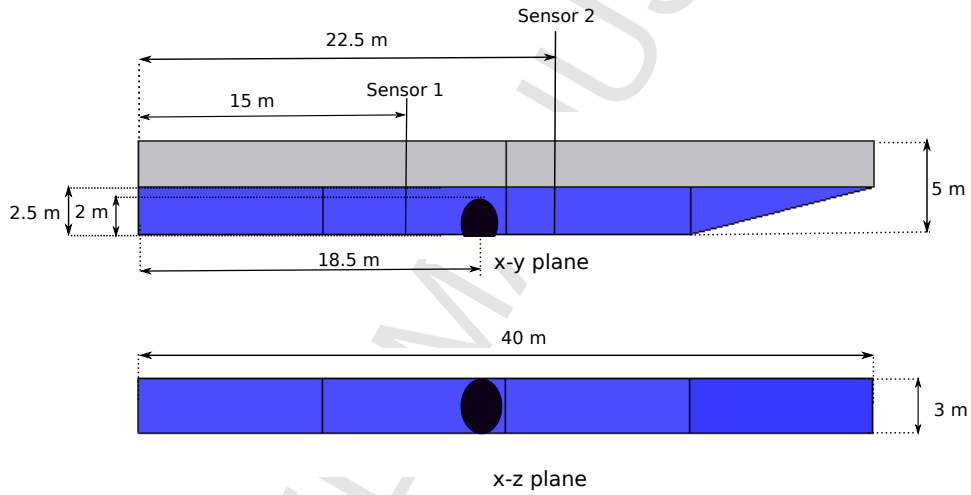


Figure 15: A schematic of a channel with a water-bag reef.

$x=18.5$ m center of a membrane balloon filled with water is located. The flexible reef domain is created by constructing a sphere with a diameter of 2.5 m, truncating it at 2 m, and finally stretching it in z direction so as to fill the entire channel in z direction. This is done in order to simplify the case, by choosing a configuration where diffraction effects can be nearly neglected. Density and viscosity of $\rho = 1000 \text{ kg/m}^3$ and $\nu = 10^{-6} \text{ Pa} \cdot \text{s}$ for both the internal and the external fluids are considered. The membrane bag has the following properties: density $\rho_m = 2000 \text{ kg/m}^3$, Young's modulus $E = 100 \text{ MPa}$, Poisson's ratio $\zeta = 0.1$ and thickness $t = 0.003 \text{ m}$.

A periodic velocity "flap-type" inlet is prescribed at the left boundary of the channel domain in order to generate waves [37]. The angular velocity (with the center of rotation located at the left down corner of the) is prescribed as:

$$\omega(t) = \omega_{max} \sin\left(\frac{2\pi}{T}t\right) \quad (76)$$

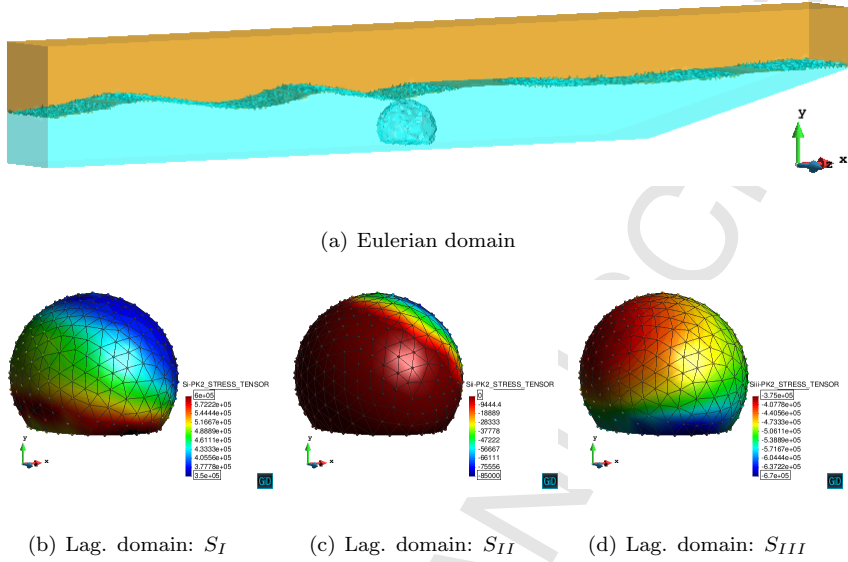


Figure 16: Water-bag reef: Eulerian and Lagrangian domains at $t=10$ s (Case 1)

The period T is set to 3 s. Two angular velocity amplitudes are considered:

- Case 1: maximum angular velocity $\omega_{max} = 0.54$ r/s.
- Case 2: maximum angular velocity $\omega_{max} = 1.08$ r/s.

Two "sensors" for recording the location of the free surface are placed at $x=15$ m (in front of the reef) and at $x=22.5$ m (behind the reef). The free surface evolution of the external fluid has been captured using the Level Set method [38] following the implementation described in [39].

A snapshot of the Eulerian domain taken at $t=10$ s is shown for Case 1 in Fig. 16(a). The corresponding flexible reef configuration and the distribution of the principal PK2 stresses S_I , S_{II} and S_{III} are shown in Fig. 16 (b,c,d).

Figs. 17 and 18 display the evolution of the wave height at sensors 1 and 2, respectively. The results computed in the absence and in the presence of the water-bag reef are shown for each case. In case of no obstacle, the average incident wave height $H_{i1} \approx 0.24$ m for Case 1 and $H_{i2} = 0.34$ m for Case 2.

The results recorded at sensor 2 provide the following estimation of the transmitted wave heights: $H_{t1} \approx 0.155$ and $H_{t2} \approx 0.175$ m. Thus the transmission coefficients for the considered cases are: $K_{t1} \approx 0.65$ and $K_{t2} \approx 0.52$, respectively.

Analyzing the free surface height recorded at Sensor 1 one can see that the incident wave height slightly diminishes in the presence of the reef, which occurs due to the reflection caused by the reef.

Overall, one can see that in both cases the presence of the submerged flexible reef leads to a decrease in the wave height and, therefore, the wave energy. In

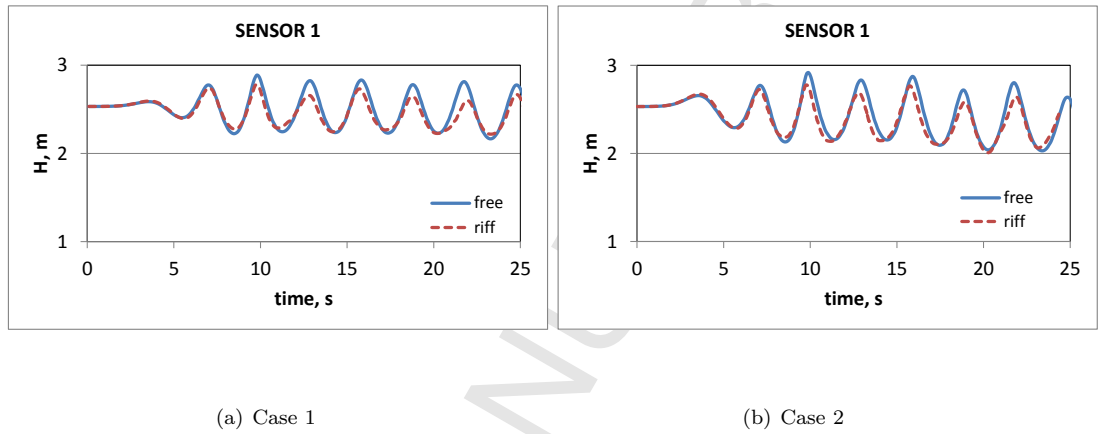


Figure 17: Water-bag reef. Time evolution of free surface height at Sensor 1

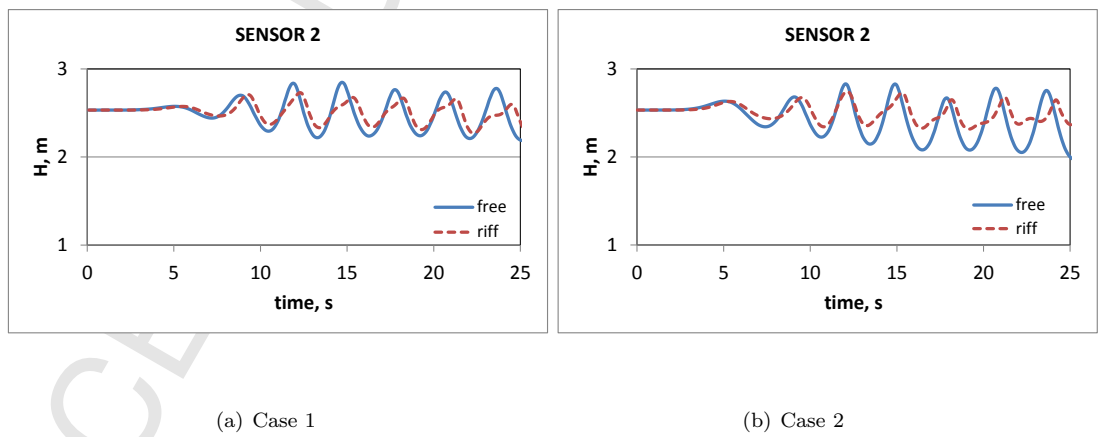


Figure 18: Water-bag reef. Time evolution of free surface height at Sensor 2

the second case, when the free water surface reaches the top of the reef, the transmitted wave completely loses its perfect sinusoidal shape.

Empirical expressions for predicting the transmission coefficients for solid trapezoidal reefs were proposed in [40], [41]. These are defined in terms of the immersion depth of the reef R_c and the average "free" wave height H_f (i.e. estimated far from the reef).

- $K_t = 0.8$, for $-2 < \frac{R_c}{H_f} < -1.13$
- $K_t = 0.46 - 0.3\frac{R_c}{H_f}$, for $-1.13 < \frac{R_c}{H_f} < 1.2$
- $K_t = 0.1$, for $1.2 < \frac{R_c}{H_f} < 2.0$

These relations have been obtained from multiple experiments carried out considering real structures. Application of the above expressions leads to $K_t \approx 0.8$ for both cases here considered. Clearly, the mentioned empirical formula cannot be applied in a straight-forward way to the problem under consideration. However, they generally indicate that when the wave height and the immersion depth are similar, the transmission coefficient decreases as the wave height increases. This trend is observed in the cases solved here.

5. Summary and conclusions

In this paper a model for solving fluid-membrane interaction problems has been proposed. The main novelty of the model consisted in an ad-hoc kinematic framework, where a monolithic Lagrangian fluid-membrane model is embedded into an Eulerian external fluid model. The overall model offers a robust, efficient and easy-to-implement numerical methodology for solving problems involving airbags or water-bags and their interaction with the surrounding fluids.

The advantages of the proposed embedded approach versus the fully Lagrangian approaches previously proposed by the authors are

- natural representation of discontinuities across the membrane. No duplication of degrees of freedom is necessary due to the proposed partitioning.
- restricting re-meshing to the interior fluid only by adopting a fixed grid approach for the external fluid. In many practical applications the surrounding fluid constitutes the major part of the computational domain. Thus the proposed approach considerably reduces the computational cost due to re-meshing.

Comparing with the former embedded approaches, where the entire fluid domain (internal and external) is modeled on a single mesh, while the membrane is solved by a separate Lagrangian solver, the proposed approach has the following benefits:

- improved computational efficiency due to splitting the original problem into two subproblems of similar complexity (external fluid and internal fluid+membrane). Standard embedded methods lead to a computationally expensive fluid problem (entire 3D fluid domain (external and internal)) and a cheap membrane problem (2D).
- capability of efficiently modeling problems with large difference in properties of the internal and external fluids due to the proposed partitioning. When both fluids are solved in a single system (as in standard embedded approaches), large properties differences (viscosity, density) result in an impoverished system conditioning.
- interface discontinuity representation without elemental shape function enrichment necessary for discontinuity representation when applying standard embedded approaches.

The method is, however, suitable for problems with closed membrane domains only. Thus, cases involving parachutes or sails cannot be directly solved with the proposed model.

Application of the model to problems characterized by steady-state and transient solutions has been shown. The model has been validated by comparing the simulation results with data available in the literature and with analytic solutions. The model has been also applied to a problem of engineering interest related to the use of water-bag reefs for bay protection. It has been shown that such flexible reefs lead to a wave energy reduction, similar to the one caused by conventional submerged concrete structures.

Acknowledgements

The present work has been partially supported by the ICEBREAKER Proof-of-Concept Grant of European Research council as well as the COMETAD project of the National RTD Plan (ref. MAT2014-60435-C2-1-R), Spanish *Ministerio de Economía y Competitividad* and the NICOP project of the Office of Naval Research Global. The corresponding author would like to express his gratitude to Drs. R. Flores, G. Casas and M.A. Celigueta for their valuable advice for modeling some of the examples presented in this work.

- [1] J.T. Oden and T. Sato. Finite strains and displacements of elastic membranes by the finite element method. *International Journal of Solids and Structures*, 3(4):471–488, 1967.
- [2] A. Ibrahimbegović and F. Gruttmann. A consistent finite element formulation of nonlinear membrane shell theory with particular reference to elastic rubberlike material. *Finite elements in analysis and design*, 13(1):75–86, 1993.

- [3] F. Gruttmann and R.L. Taylor. Theory and finite element formulation of rubberlike membrane shells using principal stretches. *International Journal for Numerical Methods in Engineering*, 35(5):1111–1126, 1992.
- [4] K.-U. Bletzinger, R. Wüchner, F. Daoud, and N. Camprubí. Computational methods for form finding and optimization of shells and membranes. *Computer Methods in Applied Mechanics and Engineering*, 194(30):3438–3452, 2005.
- [5] Narges Dialami and Farhang Daneshmand. Natural neighbor galerkin method for deflection analysis of inflatable structures. *Engineering Computations*, 26(4):440–456, 2009.
- [6] E. Van Brummelen. Added mass effects of compressible and incompressible flows in fluid-structure interaction. *Journal of Applied mechanics*, 76(2):021206, 2009.
- [7] S. Idelsohn, F. Del Pin, R. Rossi, and E. Oñate. Fluid–structure interaction problems with strong added-mass effect. *International journal for numerical methods in engineering*, 80(10):1261–1294, 2009.
- [8] G. Hou, J. Wang, and A. Layton. Numerical methods for fluid-structure interaction a review. *Commun. Comput. Phys*, 12(2):337–377, 2012.
- [9] W. McMaster. Computer codes for fluid-structure interactions. *American Society of Mechanical Engineers*, 1, 1984.
- [10] H. Koivurova and A. Pramila. Nonlinear vibration of axially moving membrane by finite element method. *Computational Mechanics*, 20(6):573–581, 1997.
- [11] Y. Fan and J. Xia. Simulation of 3d parachute fluid–structure interaction based on nonlinear finite element method and preconditioning finite volume method. *Chinese Journal of Aeronautics*, 27(6):1373–1383, 2014.
- [12] U. Kuettler and W. Wall. Fixed-point fluid-structure interaction solvers with dynamic relaxation. *Computational Mechanics*, 43:61–72, 2008.
- [13] J. Bonet, R. Wood, J. Mahaney, and P. Heywood. Finite element analysis of air supported membrane structures. *Computer methods in applied mechanics and engineering*, 190(5):579–595, 2000.
- [14] P. Ryzhakov, R. Rossi, S. Idelsohn, and E. Oñate. A monolithic Lagrangian approach for fluid-structure interaction problems. *Journal of Computational Mechanics*, 46/6:883–399, 2010.
- [15] R. Rossi, P. Ryzhakov, and E. Oñate. A monolithic fe formulation for the analysis of membranes in fluids. *Spatial structures*, 24(4):205–210, 2009.

- [16] K. Kamran, R. Rossi, E. Oñate, and S. Idelsohn. A compressible lagrangian framework for modeling the fluid–structure interaction in the underwater implosion of an aluminum cylinder. *Mathematical Models and Methods in Applied Sciences*, 23(02):339–367, 2013.
- [17] P.B. Ryzhakov, J. Marti, S.R. Idelsohn, and E. Oñate. Fast fluid–structure interaction simulations using a displacement-based finite element model equipped with an explicit streamline integration prediction. *Computer Methods in Applied Mechanics and Engineering*, 315:1080–1097, 2017.
- [18] P. Ryzhakov, E. Oñate, R. Rossi, and S. Idelsohn. Improving mass conservation in simulation of incompressible flows. *Int. Jour. for Num.Methods. in Eng.*, 2012. early view, published online 29/03/2012.
- [19] Pavel Ryzhakov, Riccardo Rossi, Adria Viña, and E Oñate. Modelling and simulation of the sea-landing of aerial vehicles using the particle finite element method. *Ocean engineering*, 66:92–100, 2013.
- [20] C. Antoci, M. Gallati, and S. Sibilla. Numerical simulation of fluid–structure interaction by SPH. *Computers & Structures*, 85(11):879–890, 2007.
- [21] Q. Yang, V. Jones, and L. McCue. Free-surface flow interactions with deformable structures using an SPH–FEM model. *Ocean Engineering*, 55:136–147, 2012.
- [22] P. Ryzhakov, J. Cotela, R. Rossi, and E. Oñate. A two-step monolithic method for the efficient simulation of incompressible flows. *International Journal for Numerical Methods in Fluids*, 74(12):919–934, 2014.
- [23] S. Idelsohn, J. Marti, A. Limache, and E. Oñate. Unified Lagrangian formulation for elastic solids and incompressible fluids. application to fluid–structure interaction problems via the PFEM. *Computer Methods in Applied Mechanics and Engineering*, 197:17621776, 2008.
- [24] Alexander N Brooks and Thomas JR Hughes. Streamline upwind/petrov-galerkin formulations for convection dominated flows with particular emphasis on the incompressible navier-stokes equations. *Computer methods in applied mechanics and engineering*, 32(1-3):199–259, 1982.
- [25] P. B Bochev, C. Dohrmann, and M. Gunzburger. Stabilization of low-order mixed finite elements for the stokes equations. *SIAM Journal on Numerical Analysis*, 44(1):82–101, 2006.
- [26] P. Ryzhakov, E. Oñate, R. Rossi, and S. Idelsohn. *Lagrangian FE methods for coupled problems in fluid mechanics*. CIMNE edition, 2010. Monograph, ISBN 978-84-96736-97-9.

- [27] P.B. Ryzhakov and A. Jarauta. An embedded approach for immiscible multi-fluid problems. *International Journal for Numerical Methods in Fluids*, 81(6):357–376, 2016.
- [28] R. Rossi. *Light-weight structures: structural analysis and coupling issues*. PhD thesis, University of Padova, 2005.
- [29] M. Lazzari, A. Saetta, and R. Vitaliani. Non-linear dynamic analysis of cable-suspended structures subjected to wind actions. *Computers & Structures*, 79(9):953–969, 2001.
- [30] T. Belytschko, W.K. Liu, B. Moran, and K. Elkhodary. *Nonlinear finite elements for continua and structures*. John Wiley & Sons, 2013.
- [31] P. Ryzhakov. A modified fractional step method for fluid–structure interaction problems. *Revista Internacional de Métodos Numéricos para Cálculo y Diseño en Ingeniería*, 33(1-2):58–64, 2016.
- [32] P. Dadvand, R. Rossi, and E. Oñate. An object-oriented environment for developing finite element codes for multi-disciplinary applications. *Archives of Computational Methods in Engineering*, 17/3:253–297, 2010.
- [33] K. Lu, M. Accorsi, and J. Leonard. Finite element analysis of membrane wrinkling. *International Journal for numerical methods in engineering*, 50(5):1017–1038, 2001.
- [34] F. Flores and E. Oñate. *Water Bags, 2D Reference Problems*. Cimne technical report edition, 2006.
- [35] A. Martínez. Modelado de la evolución de la línea de costa tras diques exentos de baja cota de coronación. 2003. PhD thesis.
- [36] L. Bricio Garberí, Negro V., J. J. Diez, and J. S. López. Diseño funcional y ambiental de diques exentos de baja cota de coronación. *Ingeniería Civil*, (158):53–61, 2010.
- [37] A. Lal and M. Elangovan. Cfd simulation and validation of flap type wave-maker. *World Academy of Science, Engineering and Technology*, 46(1):76–82, 2008.
- [38] S.J. Osher and R. P. Fedkiw. *Level Set Methods and Dynamic Implicit Surfaces*. Springer edition, 2006.
- [39] R. Rossi, A. Larese, P. Dadvand, and E. Oñate. An efficient edge-based level set finite element method for free surface flow problems. *International Journal for Numerical Methods in Fluids*, 71(6):687–716, 2013.
- [40] K. d’Angremond, J. Van Der Meer, and R. De Jong. Wave transmission at low-crested structures. In *Coastal Engineering 1996*, pages 2418–2427. 1997.

- [41] J. Van der Meer, R. Briganti, B. Zanuttigh, and B. Wang. Wave transmission and reflection at low-crested structures: Design formulae, oblique wave attack and spectral change. *Coastal Engineering*, 52(10):915–929, 2005.